



# CHORUS

This is the accepted manuscript made available via CHORUS. The article has been published as:

## Vortex-soliton complexes in coupled nonlinear Schrödinger equations with unequal dispersion coefficients

E. G. Charalampidis, P. G. Kevrekidis, D. J. Frantzeskakis, and B. A. Malomed

Phys. Rev. E **94**, 022207 — Published 10 August 2016

DOI: [10.1103/PhysRevE.94.022207](https://doi.org/10.1103/PhysRevE.94.022207)

# Vortex–soliton complexes in coupled nonlinear Schrödinger equations with unequal dispersion coefficients

E. G. Charalampidis and P. G. Kevrekidis

*Department of Mathematics and Statistics, University of Massachusetts Amherst, Amherst, Massachusetts 01003-4515, USA*

D. J. Frantzeskakis

*Department of Physics, University of Athens, Panepistimiopolis, Zografos, Athens 15784, Greece*

B. A. Malomed

*Department of Physical Electronics, School of Electrical Engineering,  
Faculty of Engineering, Tel Aviv University, Tel Aviv 69978, Israel*

We consider a two-component, two-dimensional nonlinear Schrödinger system with unequal dispersion coefficients and self-defocusing nonlinearities, chiefly with equal strengths of the self- and cross-interactions. In this setting, a natural waveform with a nonvanishing background in one component is a vortex, which induces an effective potential well in the second component, via the nonlinear coupling of the two components. We show that the potential well may support not only the fundamental bound state, but also multi-ring excited radial state complexes for suitable ranges of values of the dispersion coefficient of the second component. We systematically explore the existence, stability, and nonlinear dynamics of these states. The complexes involving the excited radial states are weakly unstable, with a growth rate depending on the dispersion of the second component. Their evolution leads to transformation of the multi-ring complexes into stable VB solitons ones with the fundamental state in the second component. The excited states may be stabilized by a harmonic-oscillator trapping potential, as well as by unequal strengths of the self- and cross-repulsive nonlinearities.

## I. INTRODUCTION

Multi-component nonlinear Schrödinger (NLS) systems emerge in a variety of contexts of optical [1] and atomic physics [2, 3]. In the former setting, they model, in particular, the interaction of waves with different carrier wavelengths [4, 5], while in atomic Bose-Einstein condensates (BECs) they apply [in the form of coupled Gross-Pitaevskii (GP) equations] to spinor (or pseudo-spinor) systems, which represent mixed condensates formed by different hyperfine states of the same atomic species [6–8], as well as to heteronuclear mixtures composed by different species [9].

In such multi-component settings, when the nonlinearity is self-defocusing (self-repulsive), a prototypical example of a one-dimensional self-trapped structure is given by dark-bright (DB) solitons. These are ubiquitous in two-component systems with the self- and cross-repulsion (alias self- and cross-phase-modulation, SPM and XPM, respectively) represented by cubic terms. Since long ago, the DB solitons have drawn much interest in nonlinear optics [10–16], including their realization in pioneering experiments reported in Refs. [17, 18]. More recently, the remarkable control available in pristine experimental settings of atomic BECs in ultracold gases, such as  $^{87}\text{Rb}$  and  $^{23}\text{Na}$ , with a multitude of available co-trapped hyperfine states, as well as in heteronuclear mixtures, such as  $^{87}\text{Rb}$ - $^{41}\text{K}$  [9], has opened a new gateway to the realization of DB solitons. Indeed, these structures were created in a multitude of state-of-the-art experiments either controllably, or spontaneously, and their pairwise interactions, as well as interactions with external potentials, were studied [19–23]. Related  $SO(2)$  rotated DB soliton states, in the form of dark-dark solitons, were also experimentally produced [24, 25].

The formation of the DB solitons is based on the fact that dark solitons are fundamental modes in single-component one-dimensional (1D) self-defocusing media. These modes, when created in one component of a two-component system, induce an effective potential well in the other component. This potential well gives rise to its fundamental bound state, i.e., the ground state (GS), which represents the bright component of the DB soliton complex. The knowledge of the explicit form of the dark soliton enables one to explore the induced potential well, which is generically of the Pöschl-Teller type [26]. It is possible to demonstrate, as done recently [27], that, if the dispersion coefficient in the second component is different from its counterpart in the first component, not only the GS, but also excited states can be trapped by the potential well in the second component. When the DB soliton states emerge at their bifurcation point, they have an infinitesimal amplitude of the bright component in the effective potential induced by the action of the SPM term. However, they can be readily continued numerically to finite values of the amplitude. Heteronuclear BEC mixtures with different atomic masses of the components provide a straightforward realization of the coupled GP equations with different dispersion coefficients (inverse atomic masses). In addition, spin-orbit coupled BECs [28]

offer the same possibility, for states that coexist in the upper- and lower-energy bands of the linear spectrum [29]. In terms of optics, a similar realization is provided by the copropagation of two beams carried by widely different wavelengths in a self-defocusing medium. Another recently developed ramification of the topic of the DB solitons in systems with unequal effective dispersion coefficients is the consideration of systems of equations with quintic SPM and cubic XPM repulsive interactions. They model the immiscibility regimes in heteronuclear binary Tonks-Girardeau (TG) gases [30], as well as BEC-TG mixtures [31].

It is natural and quite interesting to extend the concept of DB soliton states to higher dimensions. In particular, the fact that the component carrying patterns supported by nonzero background induces an effective trapping potential in the other component, remains valid in this case. In the two-dimensional (2D) setting, such patterns are well-known stable vortices [32] (vortices were studied in multi-component systems too [33]). A vortex in one component generates an effective axisymmetric potential well in the other, which may trap a bright 2D solitary wave, producing a complex that was given different names – in particular, a vortex-bright (VB) soliton [34], a half-quantum vortex [35], a filled-core vortex [36], as well as a baby Skyrmion [37]. Similar stable two-component modes are “semi-vortices” in the free 2D [38] and 3D [39] space with the attractive SPM and XPM terms, which are made stable by the spin-orbit coupling; they are composed of a bright vortex soliton in one component, and a bright fundamental one in the other.

It is important to note that the VB soliton complexes in the self-repulsive setting of a mixture of internal states of  $^{87}\text{Rb}$  atoms were created experimentally in the early work of [36]. Subsequently, their stability [34, 40] and dynamics [34, 35] have been examined theoretically. It was shown that these states feature intriguing interactions that decay with the distance  $r$  between them as  $1/r^3$  [35]. Pairs of VB soliton complexes can form bound states in atomic BECs, as shown in detail in Ref. [41].

Our objective in the present work is to consider VB soliton complexes in the system featuring repulsive SPM and XPM interactions, and different dispersion coefficients of the two components (i.e., different atomic masses in the respective coupled GP equations, or different propagation constants in the coupled NLS equations for optical beams). We aim to generate a broad set of novel families of excited complexes, with the vortex in the first component potentially trapping not only the fundamental bright solitons, but also excited radial states in the second component, represented by confined multi-ring shaped waveforms. We demonstrate that such complexes are possible in the two-component NLS/GP system. The fundamental state among them, the VB soliton complex, is generically found to be stable. On the other hand, the complexes whose bright component is represented by the excited ring-shaped modes are found to be unstable. However, varying the dispersion coefficient of the second component, we can identify scenarios where it is possible to render the corresponding instability very weak, and the associated structures very long-lived. Furthermore, if an additional harmonic-oscillator trapping potential is added to the system, which is, as a matter of fact, a mandatory ingredient of the experimental realization of the setting in BEC, we show that it is possible to render such structures completely stable in suitable parametric intervals. Lastly, we showcase basic scenarios of the instability development, inferring that the unstable (in the free space) multi-ring states are typically transformed into the stable VB fundamental ones.

The presentation in the paper is structured as follows. The model is introduced in Section II. In Sec. III, we discuss the computational analysis of the model, presenting both the numerical methods and results. Finally, in Sec. IV we summarize our findings and mention possible directions for future studies.

## II. THE MODEL AND ANALYTICAL CONSIDERATIONS

Motivated by the above-mentioned realizations in BECs and nonlinear optics, we consider the coupled defocusing GP/NLS system in  $(2+1)$  dimensions (two spatial and one temporal). In the scaled form, the system is

$$i\partial_t\Phi_- = -\frac{D_-}{2}\nabla^2\Phi_- + \gamma(g_1|\Phi_-|^2 + \sigma_{12}|\Phi_+|^2)\Phi_- + V(x,y)\Phi_-, \quad (1)$$

$$i\partial_t\Phi_+ = -\frac{D_+}{2}\nabla^2\Phi_+ + \gamma(\sigma_{12}|\Phi_-|^2 + g_2|\Phi_+|^2)\Phi_+ + V(x,y)\Phi_+, \quad (2)$$

where  $\nabla^2 = \partial_x^2 + \partial_y^2$  is the Laplacian in 2D,  $D_{\pm}$  are the dispersion coefficients,  $\gamma$  is the overall nonlinearity strength, with relative SPM and XPM interaction coefficients  $g_j$  ( $j = 1, 2$ ) and  $\sigma_{12}$ , respectively. Equations (1) and (2) include the usual parabolic trapping potential,

$$V(x,y) = \frac{1}{2}\Omega^2(x^2 + y^2), \quad (3)$$

with normalized trap strength  $\Omega$ . Fields  $\Phi_-$  and  $\Phi_+$  carry the vortex and bright-soliton components, respectively. From now on, we focus on the basic case of equal interaction coefficients,

$$g_{1,2} = \sigma_{12} = 1, \quad (4)$$

and use rescaling to fix  $D_- = \gamma = 1$ , while  $D_+ \equiv D \geq 0$  is the relative dispersion coefficient in the second component.

In the case of the binary heteronuclear BECs, coefficient  $D$  is determined by the two atomic masses,  $D = m_-/m_+$ , while in the case of the spin-orbit coupled BECs, is given by the ratio of the group-velocity dispersion coefficients, as found by the corresponding dispersion relation of the two-component branches [29]. On the other hand, in the optics model, time  $t$  is replaced by the propagation coordinate,  $z$ , in the corresponding bulk waveguide [1], and  $D$  is determined by the carrier wavelengths of the two beams,  $D = \Lambda_+/\Lambda_-$ . In particular, referring to  $^{87}\text{Ru}$ - $^7\text{Li}$  BEC mixtures, which are available to current experiments (see Ref. [42] and references therein), the relative dispersion coefficient may reach values as large as  $\simeq 12$ , and as small as  $\simeq 0.08$ . In optics, the use of materials with broadband transparency may give rise to a roughly similar range of  $D$ . However, in the case of very large or very small  $D$ , Eq. (4) is not relevant, and the analysis will need to be adjusted to other values of the SPM and XPM coefficients.

Stationary solutions to Eqs. (1)-(2) with chemical potentials  $\mu_{\pm}$  (or propagation constants  $-\mu_{\pm}$ , in terms of the optical beams) are looked for as  $\Phi_{\pm}(x, y, t) = \phi_{\pm}(x, y) \exp(-i\mu_{\pm}t)$ , reducing Eqs. (1)-(2) to the coupled system of stationary equations:

$$\mu_- \phi_- = -\frac{1}{2} \nabla^2 \phi_- + (|\phi_-|^2 + |\phi_+|^2) \phi_- + V(x, y) \phi_-, \quad (5)$$

$$\mu_+ \phi_+ = -\frac{D}{2} \nabla^2 \phi_+ + (|\phi_-|^2 + |\phi_+|^2) \phi_+ + V(x, y) \phi_+. \quad (6)$$

Further, we introduce the following *Ansätze* for the stationary fields, with real radial functions  $f_{\pm}(r)$ :

$$\phi_-(r, \theta) = f_-(r) e^{iS\theta}, \quad (7)$$

$$\phi_+(r, \theta) = f_+(r) e^{in\theta}, \quad (8)$$

where  $r = \sqrt{x^2 + y^2}$  is the radial distance,  $\theta = \tan^{-1}(y/x)$  is the polar angle, and the integer topological charges of the vortex and bright solitons are  $S$  and  $n$ , respectively. Thus, Eqs. (5)-(6) reduce to the radial equations:

$$\frac{d^2 f_-}{dr^2} + \frac{1}{r} \frac{df_-}{dr} - \frac{S^2 f_-}{r^2} - 2(f_-^2 + f_+^2 - \mu_- + V(r)) f_- = 0, \quad (9)$$

$$D \left( \frac{d^2 f_+}{dr^2} + \frac{1}{r} \frac{df_+}{dr} - \frac{n^2 f_+}{r^2} \right) - 2(f_-^2 + f_+^2 - \mu_+ + V(r)) f_+ = 0. \quad (10)$$

It should be noted in passing that in the majority of cases studied below we consider Eqs. (1)-(2), (5)-(6), as well as Eqs. (9)-(10) in the absence of the trapping potential. Therefore, we set  $V(r) = 0$ , unless it is said otherwise.

As indicated above, our fundamental premise, similar to that adopted in the study of the 1D setting in Ref. [27], is that the dark mode (dark soliton in 1D, and vortex in this present case) of the defocusing NLS equation induces an effective potential (via the XPM interaction) in the other component, which in turn gives rise to trapping of the bright-soliton state in it. Thus, Eq. (5) and, in particular, its radial version simplifies to the single-component equation,

$$\nabla_r^2 f_- - \frac{S^2 f_-}{r^2} - 2(f_-^2 - \mu_-) f_- = 0, \quad (11)$$

in the absence of the bright component, i.e., for  $f_+ = 0$ ; here,  $\nabla_r^2 = d^2/dr^2 + r^{-1}d/dr$  is the radial part of the Laplace operator. Equation (11) was solved numerically via fixed-point (Newton-Raphson) iterations (see Sec. III below for details on the computational methods employed in this work). Suitable approximate solutions for the vortical waveform are known too (see, e.g. Ref. [43]), and they may be useful as initial guesses for the iterative process described numerically below. From here on, we assume that this iterative process converges to a radial solution for the vortex. This is different from the 1D case, where the dark soliton is available in the commonly known analytical form, and the Pöschl-Teller potential [26] that it induces in the other component is analytically tractable [27]. In the 2D system presented in this work, the analysis has to be completed numerically.

Thus, the resulting vortex profile  $f_-$  (or  $\phi_-$ , for given  $S$ ) of Eq. (11) plays the role of the background for the weak component  $f_+$  (or  $\phi_+$ , for given  $n$ ). As follows from Eq. (11), the amplitude of the background for the vortex is

$$f_-(r \rightarrow \infty) = \sqrt{\mu_-} \quad (12)$$

which (upon rescaling) is set to be  $\mu_- = 1$ , in our numerical computations below. Then, when the solution for the component  $f_+$  bifurcates from its linear limit corresponding to  $f_+ \rightarrow 0$ , the linearized form of Eq. (10) amounts to an eigenvalue problem

$$\mathcal{L}f_+ = \mu_+ f_+, \quad (13)$$

for known  $f_-$ , where  $\mathcal{L} = -(D/2) (\nabla_r^2 - n^2/r^2) + f_-^2$  is a linear operator and  $(\mu_+, f_+)$  is the eigenvalue-eigenvector pair. Armed with the set of profiles for  $f_{\pm}$  obtained from Eqs. (11) and (13) as initial guesses, we utilize an iterative scheme towards the solution of the full nonlinear system of Eqs. (9)-(10) (see Sec. III below for details).

It is natural to expect that nonlinear solutions to Eqs. (9)-(10) and (5)-(6), corresponding to the ground and excited states in the linear limit for component  $f_+$ , emerge (bifurcate) at some critical values of  $D$  with the corresponding eigenvalues  $\mu_+$  of the linear problem based on Eq. (13). These values are found below by performing numerical continuations over the aforementioned parameters.

### III. NUMERICAL ANALYSIS

#### A. Computational methods

In this section, numerical results are presented for the coupled GP/NLS system (1)-(2). Our analysis addresses the *existence, stability, and dynamical evolution* of the nonlinear modes under consideration. As concerns the existence and stability, a parametric continuation is performed in chemical potential  $\mu_+$  of the bright component for given values of relative dispersion coefficient  $D$ . The corresponding states are thus identified along with their stability spectra. When the solutions are predicted to be stable, this is verified by direct simulations. For unstable states, the simulations aim to reveal the eventual states into which they are spontaneously transformed.

In our numerical computations, a 1D uniform spatial grid is employed along the radial direction, consisting of  $N$  points  $r_j = j\delta r$ , with  $j = 1, \dots, N$  and lattice spacing  $\delta r = 0.05$ . The origin is located at  $j = 0$ , whereas the domain cut-off ( $r_{\max}$ ) is set at  $j = N + 1$  (from now on, we fix  $r_{\max} = 50$ ). In this way, both fields  $f_{\pm}(r)$  are replaced by their discrete counterparts on the spatial grid,  $f_{j,\pm} = f_{\pm}(r_j)$ . Then, the radial Laplacian  $\nabla_r^2$  in Eqs. (9)-(10), (11) and (13) is replaced by second-order central-finite-difference formulas for the first and second derivatives. To secure a well-posed problem, we employ the boundary conditions (BCs)  $f_-(r = 0) = 0$  and  $df_-/dr(r \rightarrow \infty) = 0$  for the vortex soliton component, and  $df_+/dr(r = 0) = 0$  and  $f_+(r \rightarrow \infty) = 0$  for the bright-soliton one. In particular, the zero-derivative (Neumann) BCs are incorporated into the internal discretization scheme using the first-order backward and forward difference formulas, respectively. Essentially, the zero-derivative (no-flux) BCs are enforced by requiring  $f_{N+1,-} = f_{N,-}$  and  $f_{0,+} = f_{1,+}$ , whereas  $f_{0,-} = f_{N+1,+} = 0$ , as per the corresponding homogeneous Dirichlet BCs.

The starting point is Eq. (11) for radial profile  $f_-$  of the vortex component. From now on, we fix the vorticities of the vortex- and bright-soliton components to be  $S = 1$  and  $n = 0$ , respectively, given that our emphasis is on VB soliton complexes. We solve Eq. (11) by means of the standard Newton-Raphson method, which converges to a vortex profile as long as a sufficiently good initial guess is used. An example of an input, which ensures both the convergence and compliance with error-tolerance criteria, is  $f_-(r) = \tanh r$ . The resulting converged waveform for different vorticities  $S \geq 1$  features the correct asymptotic form at  $r \rightarrow 0$ ,  $f_-(r \rightarrow 0) \sim r^S$ , and its density asymptotes to  $\mu_-$  for large  $r$ . Subsequently, with background field  $f_-$  at hand, we solve the eigenvalue problem (13) numerically, to obtain the corresponding bright component,  $f_+(r)$ , with an infinitesimal amplitude, along with the associated chemical potential,  $\mu_+$ . Our study is organized according to the order of the bound states (the ground state, first excited state, and so on), and the value of  $D$ . Specifically, we determine chemical potentials  $\mu_+$  corresponding to one of the lower eigenstates (the ground state corresponds to lowest  $\mu_+$ , the first excited state pertains to the second lowest eigenvalue, and so on) and the corresponding bright eigenfunction  $f_+$  is obtained afterwards. This way, the fully nonlinear self-trapped states of system (9)-(10) can be obtained with the help of the Newton-Raphson scheme, the seed for the respective iterations consisting of the vortex radial profile  $f_-(r)$  together with the eigenvalue-eigenvector pair  $(\mu_+, f_+)$ . Essentially, the seed fed to our nonlinear solver originates from the underlying linear limit discussed in the previous Section. In addition, we trace the stationary solutions, for a given value of dispersion coefficient  $D$ , by performing a numerical continuation with respect to chemical potential  $\mu_+$ , by dint of the *sequential continuation* method, i.e., using the solution for given  $\mu_+$ , found by the solver, as the seed for the next continuation step. We are thus able to numerically determine not only the range of dispersion coefficient  $D$ , but also the range of chemical potential  $\mu_+$  for each case of interest. The validity of the stationary solutions produced by the Newton-Raphson code has been corroborated upon using a collocation method [44] for solving boundary value problems.

Having identified the stationary states, we turn to the study of their stability. Motivated by the decomposition described in Ref. [45], we start with the generalized perturbation ansatz around stationary solutions, writing in the polar coordinates:

$$\tilde{\Phi}_-(r, \theta, t) = e^{-i\mu_- t} e^{iS\theta} \left\{ f_- + \varepsilon \sum_{|m|=0}^{\infty} \left[ a_m(r) e^{\lambda t} e^{im\theta} + b_m^*(r) e^{\lambda^* t} e^{-im\theta} \right] \right\}, \quad (14)$$

$$\tilde{\Phi}_+(r, \theta, t) = e^{-i\mu_+ t} e^{in\theta} \left\{ f_+ + \varepsilon \sum_{|m|=0}^{\infty} \left[ c_m(r) e^{\lambda t} e^{im\theta} + d_m^*(r) e^{\lambda^* t} e^{-im\theta} \right] \right\}, \quad (15)$$

where  $\lambda$  is a (complex) eigenvalue,  $\varepsilon$  is an infinitesimal amplitude of the perturbation, and the asterisk stands for complex conjugate. We insert Eqs. (14)-(15) into the radial version of Eqs. (1)-(2) and thus obtain, at order  $\varepsilon$ , an eigenvalue problem in the following matrix form:

$$\tilde{\lambda} \begin{pmatrix} a_m \\ b_m \\ c_m \\ d_m \end{pmatrix} = \begin{pmatrix} A_{11} & A_{12} & A_{13} & A_{14} \\ -A_{12}^* & A_{22} & -A_{14}^* & -A_{13}^* \\ A_{13}^* & A_{14} & A_{33} & A_{34} \\ -A_{14}^* & -A_{13} & -A_{34}^* & A_{44} \end{pmatrix} \begin{pmatrix} a_m \\ b_m \\ c_m \\ d_m \end{pmatrix}, \quad (16)$$

with eigenvalues  $\tilde{\lambda} = i\lambda$ , eigenvectors  $\mathcal{V} = (a_m, b_m, c_m, d_m)^T$ , and matrix elements

$$A_{11} = -\frac{D_-}{2} \left[ \nabla_r^2 - \frac{(S+m)^2}{r^2} \right] + \gamma [2g_1 |f_-|^2 + \sigma_{12} |f_+|^2] + V - \mu_-, \quad (17)$$

$$A_{12} = \gamma g_1 (f_-)^2, \quad (18)$$

$$A_{13} = \gamma \sigma_{12} f_- (f_+)^*, \quad (19)$$

$$A_{14} = \gamma \sigma_{12} f_- f_+, \quad (20)$$

$$A_{22} = \frac{D_-}{2} \left[ \nabla_r^2 - \frac{(S-m)^2}{r^2} \right] - \gamma [2g_1 |f_-|^2 + \sigma_{12} |f_+|^2] - (V - \mu_-), \quad (21)$$

$$A_{33} = -\frac{D_+}{2} \left[ \nabla_r^2 - \frac{(n+m)^2}{r^2} \right] + \gamma [\sigma_{12} |f_-|^2 + 2g_2 |f_+|^2] + V - \mu_+, \quad (22)$$

$$A_{34} = \gamma g_2 (f_+)^2, \quad (23)$$

$$A_{44} = \frac{D_+}{2} \left[ \nabla_r^2 - \frac{(n-m)^2}{r^2} \right] - \gamma [\sigma_{12} |f_-|^2 + 2g_2 |f_+|^2] - (V - \mu_+). \quad (24)$$

As a result, the full spectrum of nonlinear solutions  $f_{\pm}$  is obtained by putting together the spectra for different integer values of  $m$ . This was done for  $m \geq 0$  only ( $m = 0, 1, 2, 3, 4$  and  $5$  in this work), since the sets of the eigenvalues for  $\pm m$  (with  $m > 0$ ) are complex conjugates. The corresponding steady state is classified as a stable one if none of the eigenvalues  $\lambda = \lambda_r + i\lambda_i$  has  $\lambda_r \neq 0$ , given the Hamiltonian nature of our system. Note that two types of instabilities can be thus identified: (i) *exponential*, characterized by a pair of real eigenvalues with  $\lambda_i = 0$ , and (ii) *oscillatory instabilities*, characterized by complex eigenvalue quartets.

Finally, the results for the spectral stability, obtained from the solution of the eigenvalue problem [see, Eq. (16)] were corroborated by means of direct simulations of the coupled GP/NLS system (1)-(2). To do so, a parallel version (using OpenMP) of the standard fourth-order Runge-Kutta method (RK4), with a fixed time-step of  $\delta t = 10^{-4}$ , was employed. The simulations were initialized at  $t = 0$  using the available stationary solutions. To obtain the latter, we employed the Newton-Raphson method in a two-dimensional rectangular domain for system (5)-(6), using the NITSOL package [46]. The 2D uniform spatial grid was built of  $N_x \times N_y$  grid points with  $N_x \equiv N_y = 251$  and resolution  $\delta x \equiv \delta y = 0.08$ . Both fields  $\phi_{\pm}(x, y)$  were replaced by their discrete counterparts on the 2D spatial grid, i.e.,  $\phi_{i,j,\pm} = \phi_{\pm}(x_i, y_j)$  with  $i = 1, \dots, N_x$  and  $j = 1, \dots, N_y$ . Then, the Laplacian on the rectangular grid is replaced by the second-order central-finite-difference formula. As mentioned above, the Neumann BCs for both fields at edges of the grid were replaced by the first-order forward and backward difference formulas. Furthermore, the steady states on the 2D Cartesian grid are obtained from the radial ones by utilizing the following standard numerical procedure. Having the 2D grid and (discrete) radial nonlinear states  $f_{j,\pm}$  at hand, we build interpolants  $f_{\pm}(r)$  using a cubic spline interpolation. Then, fields  $\phi_{\pm}(r, \theta)$  given by Eqs. (7)-(8) are constructed (for given vorticities  $S$  and  $n$ ) and transformed from polar to Cartesian coordinates,  $(r, \theta) \rightarrow (x, y)$ , by utilizing relations  $r = \sqrt{x^2 + y^2}$  and  $\theta = \tan^{-1}(y/x)$  once again. The resulting approximate solutions are fed as initial guesses to our 2D Newton-Raphson method on the Cartesian grid  $\phi_{\pm}(x, y)$ , and the resulting iteration process converges within a few steps.

Two possible initializations of the direct simulations can be distinguished. On the one hand, we initialized the dynamics in the presence of small (uniformly distributed) random perturbations with amplitude  $\varepsilon = 10^{-3}$ , added to presumably stable stationary states. An alternative approach was to initialize the evolution using the linearization ansatz (14)-(15) for unstable solutions, with  $\varepsilon = 10^{-3}$ , eigenvector  $\mathcal{V}$  and given  $m$  corresponding to a (complex) eigenvalue being responsible for the instability. The latter approach helps to stimulate the onset of the expected

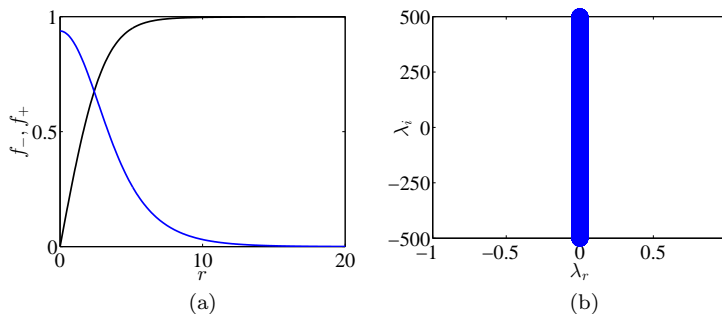


FIG. 1: (Color online) Steady-state profiles (a) of the vortex and bright soliton components (black and blue lines, respectively), and the eigenvalue spectrum (b) corresponding to a ground state with  $D = 0.6$  and  $\mu_+ = 0.95$ .

instability and observe the ensuing dynamics. The underlying eigenvector  $V$  is transformed from polar to Cartesian coordinates using the same interpolation technique mentioned previously.

## B. Numerical results

We start by considering the most fundamental state, namely the VB soliton one in Fig. 1. In this case, as well as in all the other cases that we have considered herein, we find the VB structure (shown, e.g., in the left panel of Fig. 1) to be stable, as evidenced by the absence of eigenvalues with nonzero real part in the right panel of Fig. 1.

The first excited state is shown in Fig. 2. The profile displayed in the top left panel demonstrates that the vortex retains its general structure, while featuring some changes due to the presence of a more complex spatial pattern in the bright component, with two maxima of the local density ( $|f_+|^2$ ), one at the center and another one at the periphery, separated by a notch in the form of a dark ring. The typical linearization spectrum shown in the top right panel illustrates the presence of complex instabilities. It is relevant to stress that, both in this case and in those considered below, the instabilities are associated with quartets of complex eigenvalues (even when their imaginary parts are so small that the eigenvalues may appear as real ones). The detailed spectra shown in the middle and bottom panels of the figure (cf. Figs. 2(c)-2(g)) make it clear that the lowest perturbation eigenmodes are always prone to instability, especially the ones with  $m = 0$  and  $m = 1$ . For smaller values of  $D$ , higher eigenmodes may become unstable too, and the respective instabilities may eventually (i.e., at large  $\mu_+$ ) even dominate the respective growth rate. The enhanced instability at smaller  $D$  is a natural feature to expect: indeed, as  $D$  decreases, the notch shrinks, turning into a circular quasi-1D dark soliton, whose snaking instability in two-dimensional settings is well known [8]. It is also relevant to stress that the oscillatory pattern, featured, especially, by the  $m = 0$  mode is associated with the presence of gaps in the spectrum (for our finite-domain computation), which allow the eigenmode to periodically restabilize, before it collides with another one and destabilizes anew. Similar features for other “dark” patterns have long been known (see, in particular, Ref. [47]), and are absent in the infinite-domain limit, where the relevant eigenvalue follows the envelope of the respective “trajectory” in the spectral plane.

Although our main focus in this study has been on the free space case, we now briefly touch upon the setting involving the presence of the trapping harmonic-oscillator potential. In particular, Fig. 3 displays the linearization spectra of the trapped first excited state in the bright component at  $D = 0.5$  for two different values of the trap’s strength,  $\Omega = 0.2$  and  $\Omega = 0.3$  in the left and right panels of the figure, respectively. It is evident from both panels that the trap contributes to the stability of the solution, if compared with the same branch in the free space for the same  $D$  depicted in panel (c) of Fig. 2 (see the range of the values of  $\mu_+$  as well). In addition, our findings suggest that the stability interval (i.e., the width of the interval of  $\mu_+$  in which the branch is stable), is progressively wider as  $\Omega$  increases (see the right panel of Fig. 3). Thus, gradually increasing values of the trap’s strength results in wiping out the unstable modes of the spectrum. This may be expected, as the parabolic trap makes the linearization spectrum of the system discrete (while it is continuous in the uniform space), gradually imposing a larger distance between the relevant eigenvalues, thus suppressing resonant interactions between modes that cause instabilities for such excited states [8].

Up to now, we considered the system with all the interaction (or nonlinearity) coefficients equal. It is also relevant to briefly touch upon the variation of these coefficients as in realistic atomic systems they are not precisely equal to unity; furthermore, these are parameters that can be tuned by means of the Feshbach resonances controlling interatomic scattering. In that vein, in Fig. 4 we consider the state with the first excited state in the bright component at  $\mu_+ = 0.86$  and  $D = 0.1$ . In particular, the top left and right panels correspond to the profiles for  $\sigma_{12} = 0.9$  and

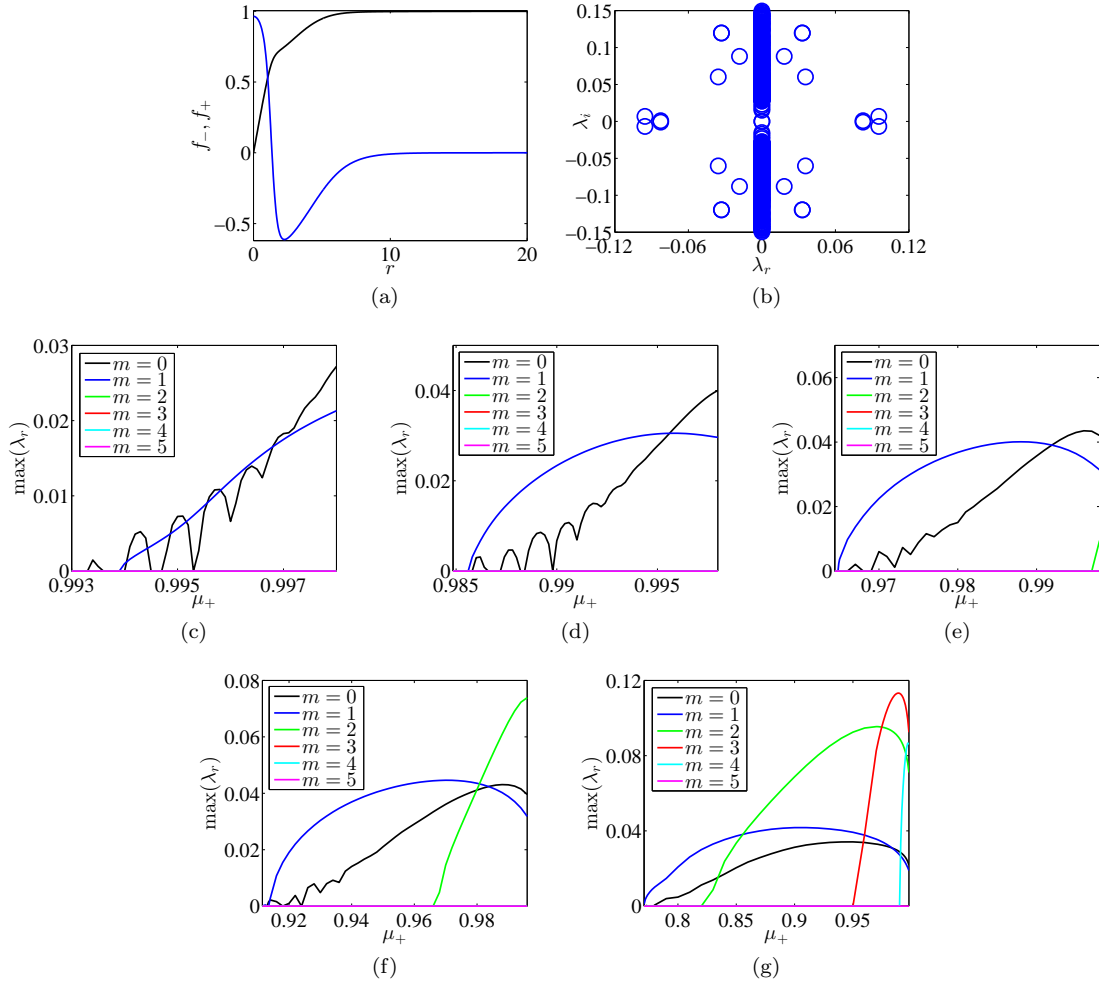


FIG. 2: (Color online) Bound states and continuation results corresponding to the first excited state in the bright component. *Top row:* (a) Stationary profiles of the vortex and bright components (the black and blue lines, respectively). (b) The corresponding eigenvalue spectrum for  $D = 0.1$  and  $\mu_{+} = 0.97$ . *Middle and bottom rows:* The largest real part of the eigenvalues as a function of  $\mu_{+}$  at various fixed values of  $D$ : (c)  $D = 0.5$ , (d)  $D = 0.4$ , (e)  $D = 0.3$ , (f)  $D = 0.2$ , and (g)  $D = 0.1$ .

$\sigma_{12} = 1.1$ , respectively, highlighting the transition from miscibility ( $\sigma_{12}^2 < g_1 g_2$ ) to immiscibility (for  $\sigma_{12}^2 > g_1 g_2$ ). The bottom panel in the figure shows the linearization spectrum in this case as a function of  $\sigma_{12}$ . In the 1D case studied in Ref. [48], it has been observed that the stability of the individual dark-bright solitons is not dramatically affected by the variation of  $\sigma_{12}$ . Similar findings are observed in the present 2D case, although the instability growth rates start decreasing, resulting in a small stability region close to the upper bound of the examined window of  $\sigma_{12}$  (see the bottom panel of Fig. 4). It should be stressed at this point that the lower bound of  $\sigma_{12}$  is determined by the fact that as  $\sigma_{12} (< 1)$  decreases, the expanding bright structure eventually reaches the domain size. On the contrary, when  $\sigma_{12} (> 1)$  increases, the bright component becomes narrower and more focused within the potential well induced by the dark structure. Furthermore, it should be pointed out that the structure decreases in amplitude with its amplitude being vanished, thus, determining the upper bound of the considered interval of  $\sigma_{12}$ .

The case of the second and third excited states in the bright component is considered in Figs. 5 and 6, respectively. The former state features a triple local density maximum in the bright component, with these maxima separated by two dark rings; the latter state has four local maxima, separated by three dark rings, as shown in the respective top left panels of the figures. One can also observe in the corresponding top right panels, which showcase typical examples of the spectral plane,  $(\lambda_r, \lambda_i)$ , of eigenvalues  $\lambda = \lambda_r + i\lambda_i$ , that the number of unstable modes is getting progressively larger with the increase of the order of the state. Some additional relevant observations regarding these figures are as follows. In Fig. 5, we observe that, for sufficiently small dispersion coefficient  $D$ , eigenvalues of higher-order perturbation modes, including ones for  $m = 3$  (and even  $m = 4$  and 5) grow fast with  $\mu_{+}$ , so that they play a dominant role in the resulting dynamics, making it different from that in more typical cases of  $m = 0$  and  $m = 1$ .

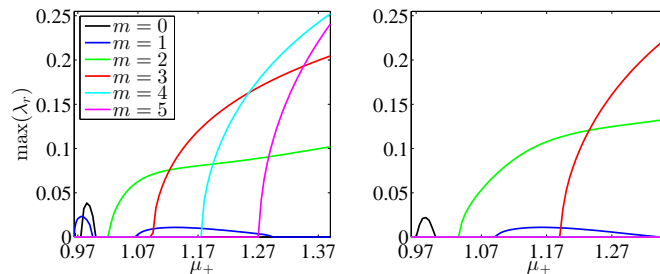


FIG. 3: (Color online) Same as Fig. 2 but in the presence of the harmonic-oscillator trap. The largest real part of the eigenvalues as a function of  $\mu_+$  at  $D = 0.5$  is depicted in the left and right panels for values of the trap's strength of  $\Omega = 0.2$  and  $\Omega = 0.3$ , respectively.

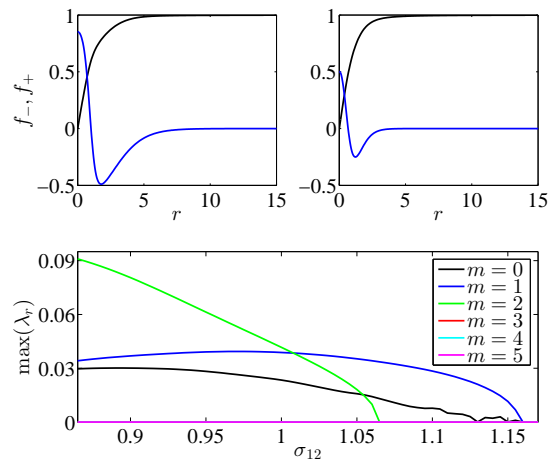


FIG. 4: (Color online) Same as Fig. 2 but for  $\mu_+ = 0.86$  and  $D = 0.1$ . *Top row*: Stationary profiles of the vortex and bright components for interaction coefficients  $\sigma_{12} = 0.9$  (left panel) and  $\sigma_{12} = 1.1$  (right panel). *Bottom row*: The largest real part of the eigenvalues as a function of interaction coefficient  $\sigma_{12}$ .

As for the waveform in Fig. 6, on the other hand, it is relevant to point out that the internal structure of the ring state has a conspicuous feedback effect on the spatial profile of the vortex. In this case, the vortex features a nearly non-monotonic profile. Here, too, higher perturbation eigenmodes, including most notably  $m = 3$ , but also, in some cases,  $m = 2$ ,  $m = 4$ , etc., may result in the largest growth rate of the instability.

Having examined the spectral stability of the different states, we now turn to direct simulations to study the evolution of these states. First, in Fig. 7, we confirm that the evolution of the fundamental VB soliton branch (where the bright component is the GS of the vortex-induced potential) does not exhibit any instability in long simulations (up to  $t = 2000$ ), even though the solution is initially perturbed.

The situation is different for the excited states. This is observed, in particular, in the evolution of the structure with the bright component represented by the first excited state displayed in Fig. 8; for the second and third excited states in the bright component the same is shown in Figs. 9 and 10, respectively. In the case of the first excited state, we see in Fig. 8 that the shape becomes elongated, resulting in the breakup of the dark density ring embedded into the bright component. As a result, the bright component gradually transforms into the GS (see, e.g., the right panel in the figure).

In the case of the second excited state shown in Fig. 9, the instability breaks the two dark rings embedded into the bright component. As a result, more norm (or power, in terms of the optical model) migrates from the outside rings towards the mode's core, pulled into the potential well induced by the vortex in the mate component. In this case, the vortex structure is only weakly affected by the instability of the bright component. Eventually (see the panel on the right side of the figure), the bright waveform builds a conspicuous maximum at the center, having shed off considerable amount of radiation. Thus, this solution approaches the GS in the bright component too, as a result of

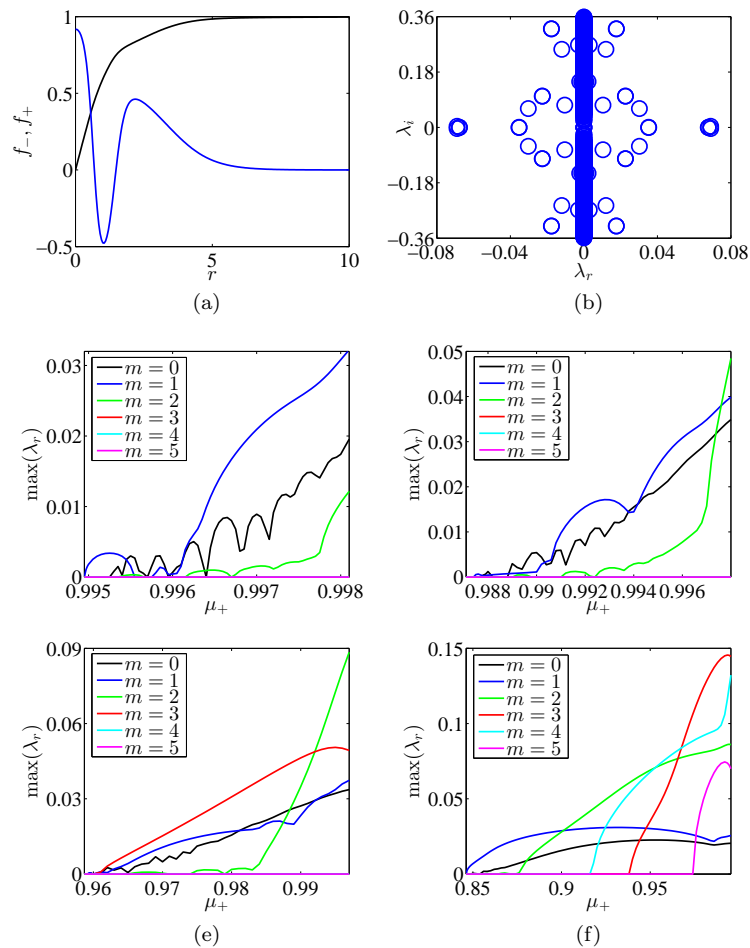


FIG. 5: (Color online) Same as Fig. 2 but for the second excited states in the bright component. *Top row:* (a) Steady-state profiles of the vortex and bright components (the black and blue lines, respectively). (b) The corresponding eigenvalue spectrum for  $D = 0.05$  and  $\mu_+ = 0.95$ . *Middle and bottom rows:* The largest real part of eigenvalues as a function of  $\mu_+$  at fixed values of  $D$ : (c)  $D = 0.2$ , (d)  $D = 0.15$ , (e)  $D = 0.1$ , and (f)  $D = 0.05$ .

the instability development.

Finally, the waveform featuring the third excited state in the bright component, characterized by a triple dark ring, exhibits complex evolution, as seen in Fig. 10. The rings get distorted, as is shown in the second column of the figure –the outer nodal line is no longer a ring, while the middle one has already been broken up. In the third column, the outer and middle dark-ring patterns are severely distorted, resulting, eventually (in the right column), in the transfer of the norm of the bright component towards the center, although surrounded by a complex pattern involving multiple nodal structures. Thus, one again sees a trend for the aggregation of the norm of the bright component at the center, implying spontaneous rearrangement of the mode into the GS. Here (as well as in the case of the bright component shaped as the first excited state), the vortex component suffers a more significant feedback from the instability development in the bright one, resulting in complex patterns observed in the dark component too. Nevertheless, the central core of the vortex remains intact, thus maintaining the effective potential trapping the bright waveform.

#### IV. CONCLUSION

We have considered the two-component GP/NLS 2D system, chiefly with equal strengths of the self- and cross-defocusing cubic nonlinearities, in which a vortex in one component induces an effective trapping potential for the other (bright) component. The system models heteronuclear BEC mixtures and the copropagation of optical beams carried by different wavelengths.

Depending on the relative dispersion parameter of the second component, the effective potential can trap not only

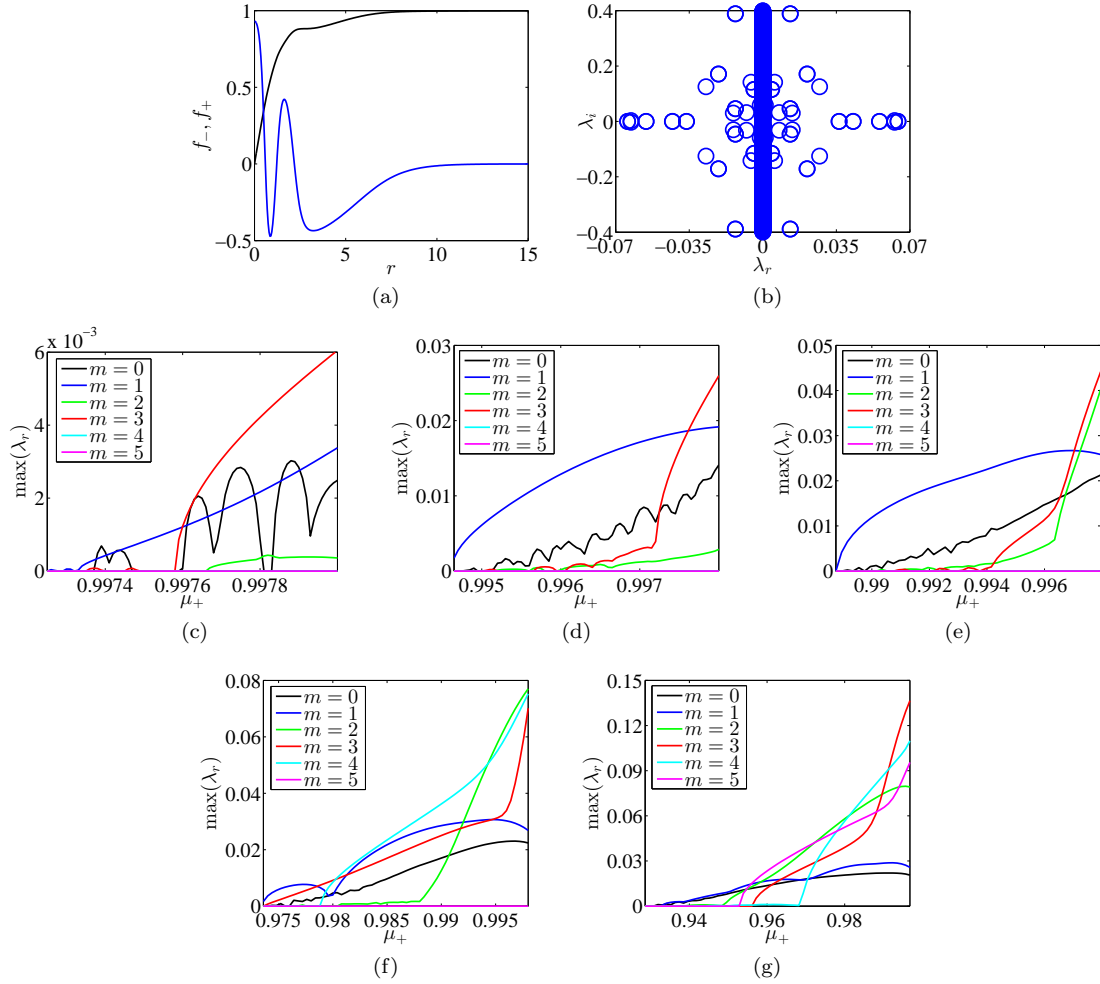


FIG. 6: (Color online) Same as Fig. 2, but for the third excited states in the bright component. *Top row:* (a) Steady-state profiles of the vortex and bright components (black and blue lines, respectively). (b) The corresponding eigenvalue spectrum for  $D = 0.04$  and  $\mu_+ = 0.9825$ . *Middle and bottom rows:* The largest real eigenvalue as a function of  $\mu_+$  at fixed values of  $D$ : (c)  $D = 0.12$ , (d)  $D = 0.1$ , (e)  $D = 0.08$ , (f)  $D = 0.06$ , and (g)  $D = 0.04$ .

the GS (ground state) in the bright component, but also the first, second and even third excited radial states. This results in complexes with multi-ring solitons in the bright component, which produce a feedback on the vortex in the first component. Among these complexes, the VB (vortex-bright) one, with the GS in the bright component, has been identified as a spectrally stable state, which is, accordingly, robust in the direct evolution.

On the other hand, the complexes with the bright component represented by the excited states are unstable, although the instability growth rate is broadly tunable, and may be made very small, by means of the variation of the relative dispersion parameter of the bright component. If the harmonic-oscillator trapping potential, which is experimentally relevant in atomic BECs, is included, the complete stabilization of the structures with the excited state of the bright component can be achieved in suitable parametric regions. The stabilization may also be provided by unequal strengths of self- and cross-repulsive interactions, as shown in Fig. 4. The spectral stability and instability, predicted by the analysis of small perturbations, were corroborated by direct simulations. In particular, the unstable complexes with the excited bright component have been shown to spontaneously rearrange into VB modes with the GS in the bright constituent.

This work paves the way for exploration of related systems. First, we actually considered only the bright component with zero vorticity,  $n = 0$  in Eq. (8) (i.e., without the angular momentum). The existence and stability of complexes with a vortical bright component,  $n \neq 0$ , is a very relevant generalization. In particular, the stability may be quite different for the same shape of the vortical bright mode with opposite signs of the vorticity,  $n = \pm 1$ , while  $S = +1$  is fixed in the first component, cf. the stability of two-component trapped modes with the *hidden vorticity* studied in Ref. [49]. Further, in this work we restrict the considerations to 2D settings, while recent work [50] has shown that 3D vortical structures are capable of trapping bright states. Another possibility, that we only briefly broached here,

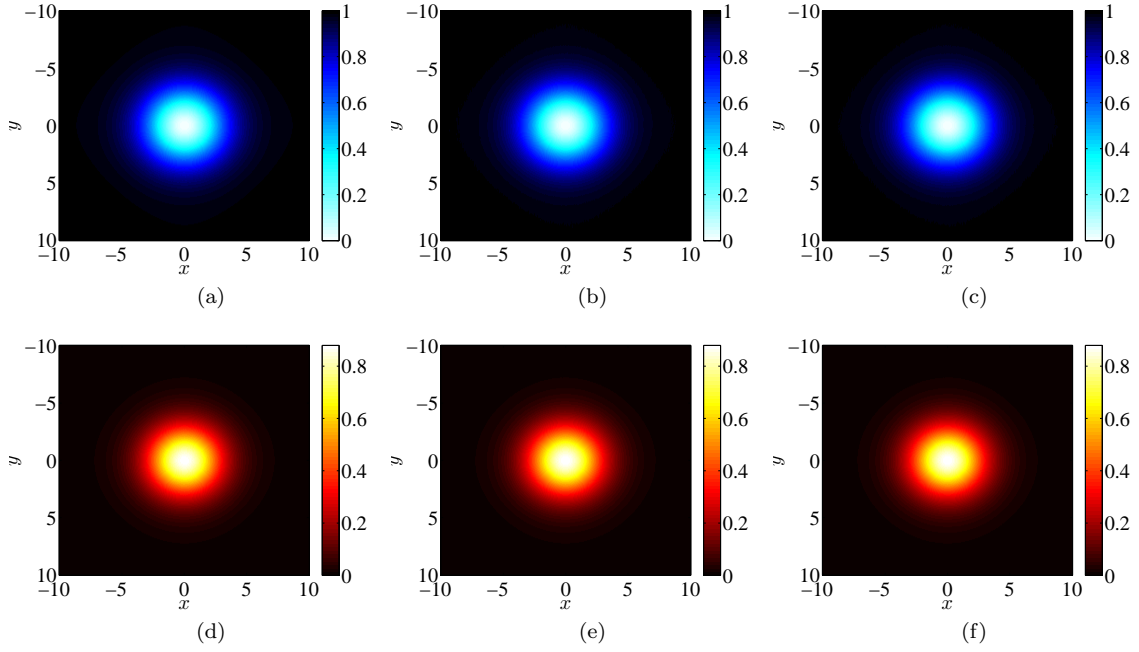


FIG. 7: (Color online) The evolution of densities  $|\Phi_-(x,t)|^2$  and  $|\Phi_+(x,t)|^2$  (the top and bottom rows), displayed at different instants of time:  $t = 0$  (left panels),  $t = 1000$  (middle panels), and  $t = 2000$  (right panels), for perturbed complexes with the bright component in the form of the ground state, at  $D = 0.6$  and  $\mu_+ = 0.95$ .

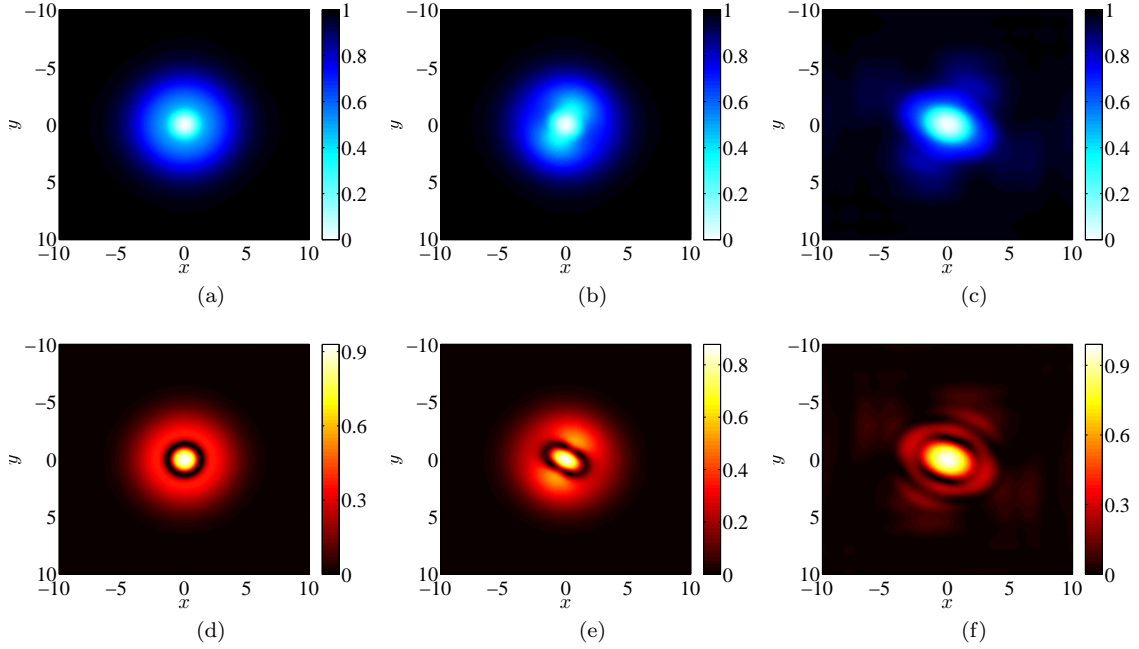


FIG. 8: (Color online) The same as Fig. 7, but for the complexes with the bright component in the form of the first excited state. Top and bottom rows display densities  $|\Phi_-(x,t)|^2$  and  $|\Phi_+(x,t)|^2$ , respectively, at  $t = 0$  (left panels),  $t = 80$  (middle panels), and  $t = 160$  (right panels) for  $D = 0.1$ ,  $\mu_+ = 0.97$  and  $m = 2$ .

is to systematically consider the states formed in the presence of the harmonic-oscillator trapping potential, which is necessarily present in experiments with atomic BECs. Finally, the present analysis is restricted to axially symmetric states trapped by the vortex-induced effective potential. It is also interesting to check if azimuthally modulated states (*azimuthons* [51]) may be produced in the present setup. Some of these extensions are presently under consideration, and will be reported elsewhere.

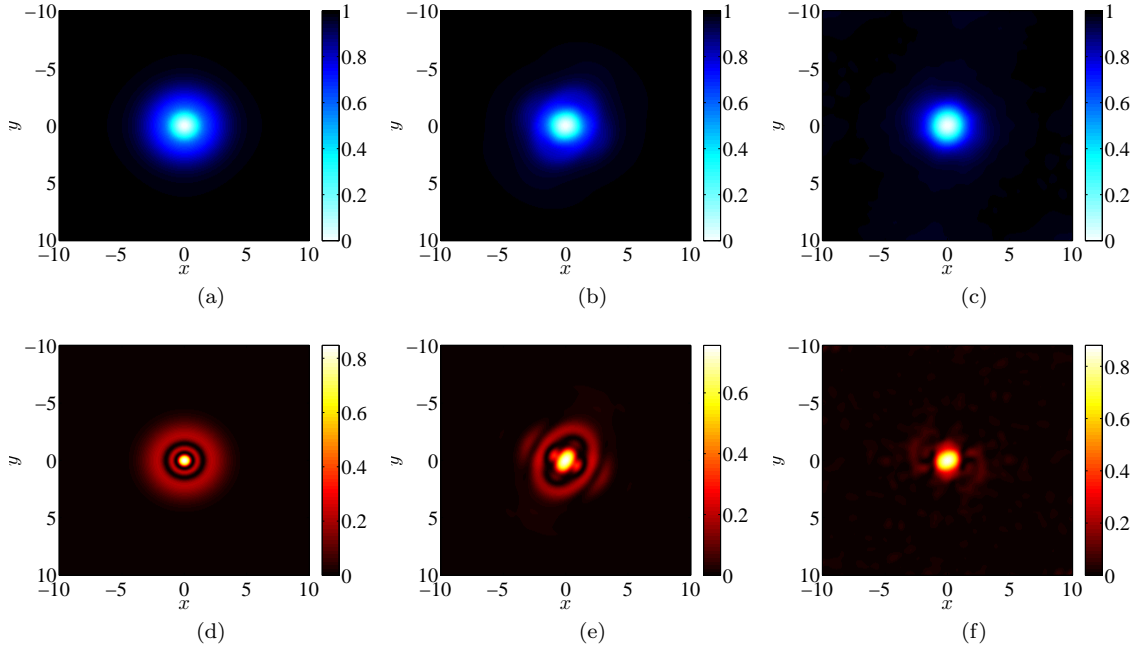


FIG. 9: (Color online) Same as Fig. 7 but for the complexes with the bright component in the form of the second excited state. Top and bottom rows display densities  $|\Phi_-(x,t)|^2$  and  $|\Phi_+(x,t)|^2$ , respectively, at  $t = 0$  (left panels),  $t = 210$  (middle panels), and  $t = 430$  (right panels), for  $D = 0.05$ ,  $\mu_+ = 0.95$  and  $m = 2$ .

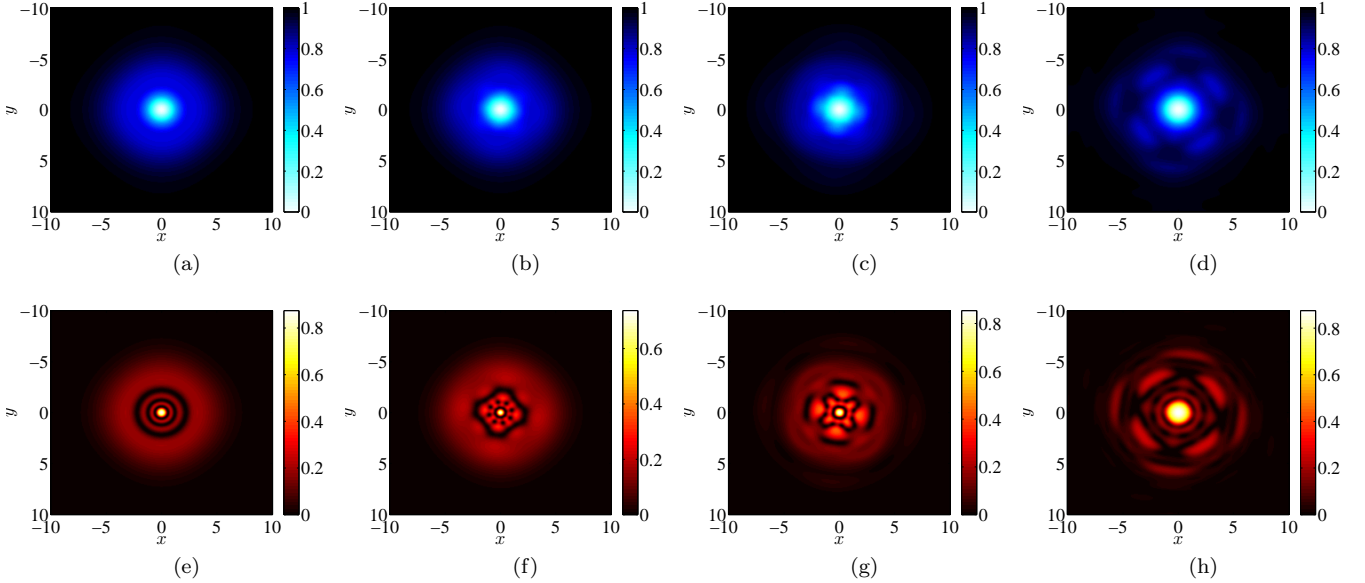


FIG. 10: (Color online) Same as Fig. 7, but for the complexes with the bright component represented by the third excited state. Top and bottom rows display densities  $|\Phi_-(x,t)|^2$  and  $|\Phi_+(x,t)|^2$ , respectively, at  $t = 0$  (panels (a) and (e)),  $t = 130$  (panels (b) and (f)),  $t = 180$  (panels (c) and (g)), and  $t = 230$  (panels (d) and (h)), for  $D = 0.04$ ,  $\mu_+ = 0.9825$  and  $m = 4$ .

### Acknowledgments

E.G.C. and P.G.K. gratefully acknowledge support from the US-AFOSR under grant FA9550-12-10332. E.G.C. is indebted to the Department of Physical Electronics, School of Electrical Engineering at the Tel Aviv University for hospitality. This author thanks Hans Johnston (UMass) for providing help in connection with the parallel computing performed in this work. P.G.K. acknowledges support from the National Science Foundation under Grant DMS-1312856 and from FP7-People under Grant No. IRSES-605096. The work of D.J.F. was partially supported by the

Special Account for Research Grants of the University of Athens. The work of P.G.K., E.G.C., and B.A.M. was supported in part by the U.S.-Israel Binational Science Foundation through Grant No. 2010239.

- 
- [1] Yu. S. Kivshar and G. P. Agrawal, *Optical Solitons: from fibers to photonic crystals*, Academic Press (San Diego, 2003).
- [2] C. J. Pethick and H. Smith, *Bose-Einstein condensation in dilute gases* (Cambridge University Press, Cambridge, 2002).
- [3] L. P. Pitaevskii and S. Stringari, *Bose-Einstein Condensation* (Oxford University Press, Oxford, 2003).
- [4] S. V. Manakov, Sov. Phys. JETP **38**, 248 (1974).
- [5] V. E. Zakharov and S. V. Manakov, Sov. Phys. JETP **42**, 842 (1976).
- [6] Y. Kawaguchi and M. Ueda, Phys. Rep. **520**, 253 (2012).
- [7] D. M. Stamper-Kurn and M. Ueda, Rev. Mod. Phys. **85**, 1191 (2013).
- [8] P. G. Kevrekidis, D. J. Frantzeskakis, and R. Carretero-González, *The Defocusing Nonlinear Schrödinger Equation* (SIAM, Philadelphia, 2015).
- [9] G. Thalhammer, G. Barontini, L. De Sarlo, J. Catani, F. Minardi, and M. Inguscio, Phys. Rev. Lett. **100**, 210402 (2008).
- [10] D. N. Christodoulides, Phys. Lett. A **132**, 451 (1988).
- [11] V. V. Afanasjev, Yu. S. Kivshar, V. V. Konotop, and V. N. Serkin, Opt. Lett. **14**, 805 (1989).
- [12] Yu. S. Kivshar and S. K. Turitsyn, Opt. Lett. **18**, 337 (1993).
- [13] R. Radhakrishnan and M. Lakshmanan, J. Phys. A: Math. Gen. **28**, 2683 (1995).
- [14] A. V. Buryak, Yu. S. Kivshar, and D. F. Parker, Phys. Lett. A **215**, 57 (1996).
- [15] A. P. Sheppard and Yu. S. Kivshar, Phys. Rev. E **55**, 4773 (1997).
- [16] Q.-H. Park and H. J. Shin, Phys. Rev. E **61**, 3093 (2000).
- [17] Z. Chen, M. Segev, T. H. Coskun, D. N. Christodoulides, and Yu. S. Kivshar, J. Opt. Soc. Am. B **14**, 3066 (1997).
- [18] E. A. Ostrovskaya, Yu. S. Kivshar, Z. Chen, and M. Segev, Opt. Lett. **24**, 327 (1999).
- [19] C. Becker, S. Stellmer, P. Soltan-Panahi, S. Dörscher, M. Baumert, E.-M. Richter, J. Kronjäger, K. Bongs, and K. Sengstock, Nature Phys. **4**, 496 (2008).
- [20] C. Hamner, J. J. Chang, P. Engels, and M.A. Hoefer, Phys. Rev. Lett. **106**, 065302 (2011).
- [21] S. Middelkamp, J. J. Chang, C. Hamner, R. Carretero-González, P. G. Kevrekidis, V. Achilleos, D. J. Frantzeskakis, P. Schmelcher, and P. Engels, Phys. Lett. A **375**, 642 (2011).
- [22] D. Yan, J. J. Chang, C. Hamner, P. G. Kevrekidis, P. Engels, V. Achilleos, D. J. Frantzeskakis, R. Carretero-González, and P. Schmelcher, Phys. Rev. A **84**, 053630 (2011).
- [23] A. Álvarez, J. Cuevas, F. R. Romero, C. Hamner, J. J. Chang, P. Engels, P. G. Kevrekidis, and D. J. Frantzeskakis, J. Phys. B **46**, 065302 (2013).
- [24] M.A. Hoefer, J. J. Chang, C. Hamner, and P. Engels, Phys. Rev. A **84**, 041605(R) (2011).
- [25] D. Yan, J. J. Chang, C. Hamner, M. Hoefer, P. G. Kevrekidis, P. Engels, V. Achilleos, D. J. Frantzeskakis, and J. Cuevas, J. Phys. B: At. Mol. Opt. Phys. **45**, 115301 (2012).
- [26] L.D. Landau and E.M. Lifshitz, *Quantum Mechanics* (Nauka Publishers, Moscow, 1989).
- [27] E. G. Charalampidis, P. G. Kevrekidis, D. J. Frantzeskakis, and B. A. Malomed, Phys. Rev. E **91**, 012924 (2015).
- [28] J. Dalibard, F. Gerbier, G. Juzeliunas, and P. Öhberg, Rev. Mod. Phys. **83**, 1523 (2011); V. Galitski and I. B. Spielman, Nature **494**, 49 (2013).
- [29] V. Achilleos, D. J. Frantzeskakis, and P. G. Kevrekidis, Phys. Rev. A **89**, 033636 (2014).
- [30] G. Filatrella, B. A. Malomed, and M. Salerno, Phys. Rev. A **90**, 043629 (2014).
- [31] G. Filatrella and B. A. Malomed, New J. Phys. **18**, 025005 (2016).
- [32] G. A. Swartzlander and C. T. Law, Phys. Rev. Lett. **69**, 2503 (1992); A. Y. Bekshaev, M. S. Soskin, and M. V. Vasnnetsov, Opt. Commun. **249**, 367 (2005); A. L. Fetter, Rev. Mod. Phys. **81**, 647 (2009); K. Y. Bliokh and F. Nori, Phys. Rep. **592**, 1 (2015).
- [33] K. Kasamatsu, M. Tsubota, and M. Ueda, Int. J. Mod. Phys. B **19**, 1835 (2005).
- [34] K. J. H. Law, P. G. Kevrekidis, and L. S. Tuckerman, Phys. Rev. Lett. **105**, 160405 (2010).
- [35] M. Eto, K. Kasamatsu, M. Nitta, H. Takeuchi, and M. Tsubota, Phys. Rev. A **83**, 063603 (2011).
- [36] B. P. Anderson, P. C. Haljan, C. E. Wieman, and E. A. Cornell Phys. Rev. Lett. **85**, 2857 (2000).
- [37] R. A. Battye, N. R. Cooper, and P.M. Sutcliffe, Phys. Rev. Lett. **88**, 080401 (2002).
- [38] H. Sakaguchi, B. Li, and B. A. Malomed, Phys. Rev. E **89**, 032920 (2014).
- [39] Y.-C. Zhang, Z.-W. Zhou, B. A. Malomed, and H. Pu, Phys. Rev. Lett. **115**, 253902 (2015).
- [40] D. V. Skryabin, Phys. Rev. A **63**, 013602 (2001).
- [41] M. Pola, J. Stockhofe, P. Schmelcher, and P. G. Kevrekidis, Phys. Rev. A **86**, 053601 (2012).
- [42] R. A. Maier, W. Eisele, E. Tiemann, and C. Zimmermann, Phys. Rev. Lett. **115**, 043201 (2015).
- [43] N. G. Berloff, J. Phys. A: Math. Gen. **37**, 1617 (2004).
- [44] U. Ascher, J. Christiansen and R. D. Russell, Math. Comput. **33**, 659 (1979); ACM Trans. Math. Softw. **7**, 209 (1981).
- [45] R. Kollar and R. L. Pego, Appl. Math. Res. Express **2012**, 1 (2012).
- [46] M. Pernice and H. F. Walker, SIAM J. Sci. Comput. **19**, 302 (1998).
- [47] M. Johansson and Yu. S. Kivshar, Phys. Rev. Lett. **82**, 85 (1999).
- [48] D. Yan, F. Tsitoura, P. G. Kevrekidis, and D. J. Frantzeskakis, Phys. Rev. A **91**, 023619 (2015).

- [49] M. Brtko, A. Gammal, and B. A. Malomed, Phys. Rev. A **82**, 053610 (2010).
- [50] S. K. Adhikari, Phys. Rev. E **92**, 042926 (2015).
- [51] A. S. Desyatnikov, A. A. Sukhorukov, Yu. S. Kivshar, Phys. Rev. Lett. **95**, 203904 (2005).